

The MeerKAT 1.3 GHz Survey of the Large Magellanic Cloud

W. D. Cotton,^{1,2*} N. Rajabpour,³ M. D. Filipović,³ F. Camilo,² R. Z. E. Alsaberi,^{3,4} L. H. Bester,^{2,5}
 A. C. Bradley,³ E. J. Crawford,³ M. Ghavam,³ O. K. Khattab,³ Z. J. Smeaton,³ O. M. Smirnov,^{2,5,6}
 J. Th. van Loon,⁷ and V. Velović³

¹National Radio Astronomy Observatory, 520 Edgemont Road, Charlottesville, VA 22903, USA

²South African Radio Astronomy Observatory, Liesbeek House, River Park, Cape Town 7700, South Africa

³Western Sydney University, Locked Bag 1797, Penrith South DC, NSW 2751, Australia

⁴Faculty of Engineering, Gifu University, 1-1 Yanagido, Gifu 501-1193, Japan

⁵Centre for Radio Astronomy Techniques and Technologies (RATT), Department of Physics and Electronics, Rhodes University, Makhanda 6140, South Africa

⁶Institute for Radio Astronomy, National Institute of Astrophysics (INAF IRA), I-40129 Bologna, Italy

⁷Lennard-Jones Laboratories, Keele University, ST5 5BG, UK

Accepted XXX. Received YYY; in original form ZZZ

ABSTRACT

We present a radio-continuum survey of the Large Magellanic Cloud (LMC) using the MeerKAT telescope, describe the full-Stokes products included in the first data release, and highlight some initial results. The observations are centred at 1.3 GHz with a bandwidth of 0.8 GHz. The imaging products comprise six fields of view, each encompassing $\sim 5^\circ \times 5^\circ$, with the resulting images achieving a resolution of $8''$. The median broad-band Stokes I image root-mean-square noise value is $\sim 11 \mu\text{Jy beam}^{-1}$. The survey enables a variety of astrophysical studies, which we showcase with the presentation of a few findings. Within the LMC we identify a new supernova remnant candidate; present planetary nebulae and Wolf-Rayet stars without previous radio detections; and show the MeerKAT view of the well-known star-forming region 30 Doradus. We also present some examples of interesting foreground and background sources in the field, including the AB Dor multiple-star system, a radio ring galaxy, a possible Odd Radio Circle, and a remarkable bent-tail radio galaxy.

Key words: (galaxies:) Magellanic Clouds — radio continuum: galaxies — ISM: supernova remnants — ISM: planetary nebulae — STARS: Wolf-Rayet

1 INTRODUCTION

The Magellanic system is a nearby pair of galaxies, the Large Magellanic Cloud (LMC) and the Small Magellanic Cloud (SMC), that are interacting with the Milky Way (MW). The LMC is located at a distance of ~ 50 kpc (Pietrzyński et al. 2019), making it close enough to be resolved in detail, providing an ideal target for galactic population studies. The LMC has been observed across the entire electromagnetic spectrum, allowing the study of different objects and processes that govern galaxy properties and evolution. In particular, the LMC has been thoroughly studied at radio frequencies in the past 50 years (Clarke 1976; Large et al. 1981; Mills 1985; Griffith & Wright 1993; Filipovic et al. 1995, 1996; White et al. 1996; Filipovic et al. 1998c; Filipović et al. 1998a,d; Filipovic et al. 1998b; Kim et al. 1998, 2003; Mauch et al. 2003; Dickel et al. 2005; Hughes et al. 2007; Murphy et al. 2010; For et al. 2018; Pennock et al. 2021; Filipović et al. 2021).

The current generation of radio telescopes, including MeerKAT (Jonas & MeerKAT Team 2016), the Australian Square Kilometre Array Pathfinder (ASKAP) (Johnston et al. 2008; Hotan et al. 2021), and the Murchison Widefield Array (Tingay et al. 2013), allow for further exploration of the LMC and its properties at radio wavelengths at much improved sensitivity and resolution.

MeerKAT has already demonstrated high-resolution and sensitivity radio-continuum studies of the MW (Heywood et al. 2022) and the neighbouring SMC (Cotton et al. 2024; Khattab et al. 2025). Similarly, there have also been ASKAP surveys of both the LMC (Pennock et al. 2021) and SMC (Joseph et al. 2019).

The recent advancements in observations of the Magellanic Clouds across multiple wavelengths present a unique opportunity to investigate the diverse range of objects and processes involved in the evolution and chemical enrichment of the Interstellar Medium (ISM) (Mayer et al. 2025). The addition of MeerKAT observations can be used to enhance the understanding of objects such as supernova remnants (SNRs), planetary nebulae (PNe), and star-forming regions, as shown in Section 4.1 of this paper. Additionally, understanding the large-scale characteristics of the LMC, such as its magnetic field, is crucial to deciphering galaxy kinematics and dynamics.

We present a new MeerKAT radio-continuum survey of the LMC. This survey provides a significant improvement over the previous ASKAP survey (Pennock et al. 2021), with almost twice the resolution ($\sim 8''$ MeerKAT restoring beam vs $14'' \times 12''$ for ASKAP), much improved sensitivity, and more precise astrometry. In addition, the MeerKAT array has 64 antennas compared with ASKAP's 36, enabling improved $u-v$ coverage and overall increased image fidelity. Furthermore, MeerKAT's core-heavy configuration improves

* E-mail: bcotton@nrao.edu

Table 1. Summary of the 258.4 hours of MeerKAT observations toward the LMC, including observation date, total integration time, and block designation.

Date	Total time (hrs)	Designation
2019 Aug 24	11.5	Block 1
2019 Aug 25	10.9	Block 2
2019 Sep 03	6.7	Block 4
2019 Sep 07	6.5	Block 4
2019 Sep 13	7.8	Block 3
2019 Sep 14	11.4	Block 13
2019 Sep 15	8.6	Block 5
2019 Sep 20	11.5	Block 6
2019 Sep 27	11.5	Block 7
2019 Sep 30	11.3	Block 8
2019 Oct 03	11.3	Block 9
2019 Oct 05	5.0	Block 10
2019 Oct 06	6.7	Block 10
2019 Oct 07	5.6	Block 11
2019 Oct 08	8.5	Block 12
2019 Oct 10	6.3	Block 15
2019 Oct 12	5.9	Block 11
2019 Oct 17	3.0	Block 12
2019 Oct 18	0.7	Block 5
2019 Oct 24	11.4	Block 16
2019 Oct 25	11.4	Block 17
2019 Oct 26	8.7	Block 14
2019 Oct 28	11.2	Block 19
2019 Oct 31	5.4	Block 3
2019 Nov 01	11.6	Block 18
2019 Nov 02	11.6	Block 20
2019 Nov 03	11.3	Block 21
2019 Nov 07	10.8	Block 22
2019 Nov 08	11.2	Block 23
2019 Nov 18	3.0	Block 14

surface brightness sensitivity, particularly for extended emission and larger-scale structures.

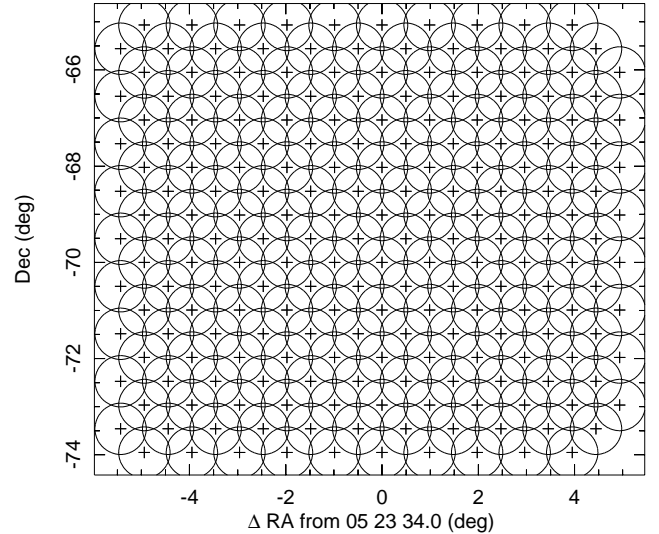
In this paper, we present the MeerKAT LMC survey and its first data release, and describe some initial scientific findings that showcase the potential for future investigations. A catalogue of point sources extracted from the survey is presented elsewhere (Rajabpour et al. 2026).

2 OBSERVATIONS

Using the South African Radio Astronomy Observatory’s MeerKAT telescope, the LMC was observed at L band (856–1712 MHz) (Jonas & MeerKAT Team 2016; Camilo et al. 2018; Mauch et al. 2020) between 24 August and 18 November 2019 (project code SSV-20180505-FC-02). The observations used 8-second integrations and 4096 channels across the band. All four polarisation correlation products were recorded.

The observations were organised into 23 blocks, with some being split over two days. Each block observed 7–8 pointing centres, which we observed cyclically in 15-minute scans interleaved with calibration scans. There was approximately one hour of integration on each pointing, which was spread over the 8–12 hours of each block to optimise the u – v coverage, with a total observing time of 258.4 hours. Table 1 provides more observing details.

Since the LMC is substantially larger than the MeerKAT antenna beam, it was covered by a mosaic of 207 pointings in a hexagonal

**Figure 1.** Coverage of the LMC centred on RA = 05 23 34.0, Dec = -69 45 22. Pluses (+) mark the pointing centres and the circles show the half-power points at mid-band.

grid centred on RA = 05 23 34.0, Dec = -69 45 22, as shown in Figure 1. The offset between pointing centres is 29′.6, giving reasonably uniform sensitivity.

3 DATA ANALYSIS

The calibration, imaging and data analysis follow that of Cotton et al. (2024) and were done using the OBIT package (Cotton 2008)¹. First, the data were downloaded from the SARAO archive². The edge channels were removed, and the data were then divided into eight equal spectral windows. Channels with strong and persistent Radio-Frequency Interference (RFI) were flagged (see Table 2) and removed from the final data set.

3.1 Calibration

The flux density, delay, bandpass and astrometric calibrator was PKS 0408–65 and the polarised calibrator was J0521+1638 (3C138). Calibration and data editing steps were interleaved. The flux density scale is set to the spectrum of PKS B1934–638 given in Reynolds (1994):

$$\log(S) = -30.7667 + 26.4908(\log \nu) - 7.0977(\log \nu)^2 + 0.605334(\log \nu)^3, \quad (1)$$

where S is the flux density in Jy and ν is the frequency in MHz.

Rajabpour et al. (2026) present a point-source catalogue obtained from this LMC survey. To assess the flux density accuracy of our survey, they compare the flux density of 39,391 point sources common between their catalogue and that of Pennock et al. (2021) from an ASKAP LMC survey at 888 MHz. Assuming a typical spectral index for synchrotron emission to scale flux densities to a common frequency, a comparison between the two sets shows a tight correlation, with the line of best fit having a slope of 1.15. Given the differences

¹ <http://www.cv.nrao.edu/~bcotton/Obit.html>

² <https://archive.sarao.ac.za/>

Table 2. MeerKAT L-band sub-band central frequencies. The table also indicates the broadband channel and the channels flagged due to RFI.

Sub-band	Frequency (MHz)	Comment
0	1295.05	Broadband
2	908.0	
3	952.3	
4	996.6	
5	1043.4	
6	1092.8	
7	1144.6	
8	1198.9	Flagged
9	1255.8	Flagged
10	1317.2	
11	1381.2	
12	1448.1	
13	1519.9	
14	1593.9	
15	1656.2	

between the surveys (e.g., in resolution), and also mindful that the ASKAP survey has an absolute flux density calibration uncertainty of 8% (Pennock et al. 2021), this is an adequate match. We judge that our flux density scale is accurate to at least $\approx 10\%$. More details can be found in Rajabpour et al. (2026).

Polarisation calibration using the “noise diode” calibration was performed at the beginning of each observing block to align the “X-Y” phases after the noise injection point. The polarised calibrator was used to determine the residual X-Y phase errors and PKS 0408–65, assumed to be unpolarised, was used to determine the instrumental polarisation. See Cotton et al. (2020) for further details.

3.2 Imaging

Stokes I, Q, U and V images were made using the OBIT task MFImage (Cotton et al. 2018). This used constant 5% fractional bandwidth sub-bands which were imaged independently but CLEANed jointly; faceting was used to account for the curvature of the sky. The sky was fully imaged to 1.2° from the pointing centre with additional facets up to 1.5° centred on sources from Mauch et al. (2003) estimated to appear brighter than 1 mJy. The central frequencies of the sub-band images are given in Table 2. The Briggs Robust factor of -1.5 (AIPS/OBIT usage) typically resulted in a resolution of $7''.5$. Stokes I CLEANing proceeded to a residual of $60 \mu\text{Jy beam}^{-1}$ or 125,000 components, Stokes Q and U to $40 \mu\text{Jy beam}^{-1}$ or 10,000 components and V was CLEANed to $20 \mu\text{Jy beam}^{-1}$ or 500 components.

All pointings had two iterations of phase self-calibration, with amplitude and phase self-calibration done if needed. Self-calibration makes only direction-independent gain corrections, which may be inadequate when there are multiple bright sources in the field. Some pointings which had images limited in dynamic range by direction-dependent effects were subjected to “Peeling” (Noordam 2004; Smirnov & Tasse 2015).

3.3 Astrometric Corrections

Various effects can lead to systematic, sub-arcsecond offsets in pointing images; these are discussed in some detail in Knowles et al. (2022). Following the approach in Cotton et al. (2024), pointing offsets were determined using MilliQuas sources (Flesch 2023).

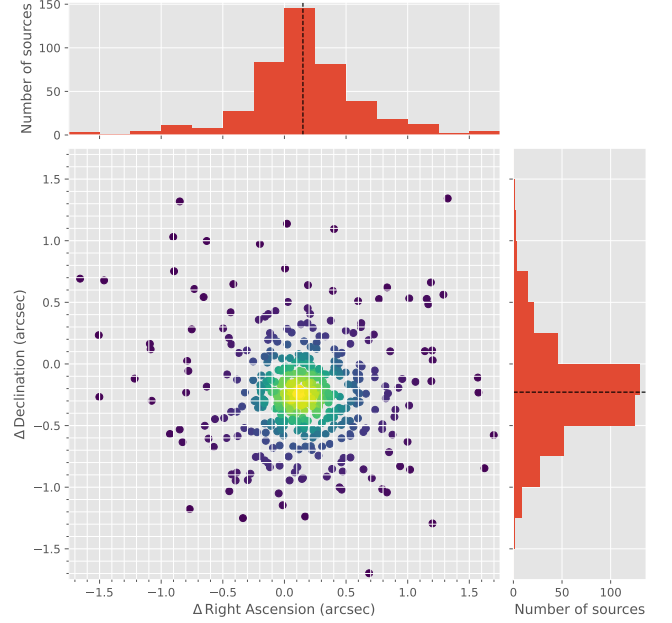


Figure 2. The differences between MilliQuas source positions and those from an early version of the MeerKAT point-source catalogue were analysed for 423 sources identified through cross-matching the two catalogues with a maximum separation radius of $4''$. The mean offsets are $\Delta\text{RA} = +0''.15 \pm 0''.02$ and $\Delta\text{Dec} = -0''.23 \pm 0''.02$.

MeerKAT sources from an early version of the point-source catalogue of Rajabpour et al. (2026) were cross-matched with MilliQuas sources within a $4''$ radius. The comparison for 423 cross-matching sources, shown in Figure 2, showed mean positional offsets of $\Delta\text{RA} = +0''.15 \pm 0''.02$ and $\Delta\text{Dec} = -0''.23 \pm 0''.02$, where the uncertainties are the errors in the mean offsets.

Only a few MeerKAT LMC survey pointings contained MilliQuas sources that could have enabled the determination of individual corrections. Therefore, a global correction derived from the above offsets was applied to all pointings.

After applying the astrometric correction, the final offsets are $\Delta\text{RA} = -0''.03 \pm 0''.5$ and $\Delta\text{Dec} = -0''.04 \pm 0''.4$, where the uncertainties are the standard deviations for the population of cross-matched sources. For more details, see Rajabpour et al. (2026).

3.4 Mosaicking

As in Cotton et al. (2024), individual pointing images were combined into a set of overlapping mosaics following the procedure described in Brunthaler et al. (2021). The overlapping pointing images are combined into a linear mosaic using:

$$M(x, y) = \frac{\sum_{i=1}^n P_i(x, y) I'_i(x, y)}{\sum_{i=1}^n P_i^2(x, y)}, \quad (2)$$

where $M(x, y)$ is the output mosaic as a function of sky coordinates, n is the number of pointing images, P_i is the antenna power gain pattern for pointing i and I' is the pointing image evaluated on the grid of the mosaic.

To ensure a constant resolution, the pointing images were convolved to $8''$ full-width at half-maximum prior to combination and the coordinates were corrected as described in Section 3.3. Individual

Table 3. LMC $5^\circ \times 5^\circ$ mosaic names and pointing centre coordinates.

Name root	RA (J2000)	Dec (J2000)
LMC_NP	04 32 21.19	-66 45 00.0
LMC_N	05 17 00.00	-66 45 00.0
LMC_NF	06 01 38.81	-66 45 00.0
LMC_SP	04 32 21.19	-71 15 00.0
LMC_S	05 17 00.00	-71 15 00.0
LMC_SF	06 01 38.81	-71 15 00.0

sub-band images were formed into mosaics, and the broadband mosaic images were derived from the sub-band mosaics. The average off-source Stokes I root mean squared (rms) was $11.3 \mu\text{Jy beam}^{-1}$, the Stokes Q and U rms was $5.9 \mu\text{Jy beam}^{-1}$ and Stokes V was $5.5 \mu\text{Jy beam}^{-1}$. The LMC was covered by 6 overlapping $5^\circ \times 5^\circ$ mosaics; their names and centre positions are given in Table 3. A representative sample is given in Figure 3.

3.5 Reference Frequency

Following Cotton et al. (2024), the reference frequency was adjusted to a common value for all broadband images using a weighted average of the sub-band images. The optimum statistical combination would use $1/\sigma_i^2$ weighting where σ_i is the off-source rms in sub-band i . However, due to the steep spectrum of noise caused by the LMC, the lower frequencies would have been severely downweighted, and so $1/\sigma_i$ weighting was used instead. This gives a reference frequency of 1295.05 MHz. To ensure this is the effective frequency, the broadband images are blanked outside the region covered by the highest sub-band; this mostly affects the edges of the LMC region. All Stokes I, Q, U and V broadband images were adjusted to this frequency.

3.6 Spectral Index

The in-band spectral indices were derived from the least-squares fit in pixels where the Stokes I values exceeded $200 \mu\text{Jy beam}^{-1}$, and where including the spectral fit did not increase the χ^2 per degree of freedom. A second set of Stokes I mosaics was produced, containing both the broadband intensity and spectral index planes, together with least-squares error estimates.

3.7 Faraday Analysis

The linear polarisation data were analysed by two techniques:

(i) RMSyn (rotation measure synthesis) — a direct search in Faraday depth looking for the maximum unwrapped polarised intensity, essentially the peak of the Faraday spectrum. This search covered $\pm 150 \text{ rad m}^{-2}$ in steps of 0.5 rad m^{-2} . This produces the unwrapped polarised intensity, the Faraday depth (also known as Rotation Measure, RM) and the Electric Vector Polarisation Vector (EVPA) at zero wavelength.

(ii) LSQ — A least squares fitting of Stokes Q and U for Rotation Measure (RM) and EVPA starting from a solution similar to that from the RMSyn method. This also produces unwrapped polarised intensity, RM, and EVPA at $\lambda = 0$, as well as error estimates for RM and EVPA.

Both of these techniques produced cubes containing multiple products; the interesting planes are: 1) RM (rad/m^2), 2) EVPA at

$\lambda = 0$ (rad), and 3) peak polarised intensity (Jy). Fractional polarisations less than of order 1% may be residual instrumental (i.e. spurious) polarisation.

3.8 Data Limitations

There are a number of limitations of the MeerKAT observations that can affect the scientific interpretation of the results in the following areas: dynamic range; largest angular size; flux density and spectral index; astrometry; polarisation. Some of these have been mitigated in the data products distributed, but will remain in the raw visibility data. A detailed discussion of the limitations as they affect the MeerKAT SMC survey, which applies equally to the LMC dataset, is given in Cotton et al. (2024).

3.9 Tarantula Deep Image

A long-track observation of the 30 Doradus region (also known as the Tarantula Nebula, see Section 4.1.1) is available under the same MeerKAT project code SSV-20180505-FC-02 and with the same observational parameters discussed in Section 2. The observation consists of alternating scans on the primary calibrator PKS 0408-65, the secondary calibrator J0506-612, and the Tarantula target field (pointing position RA = 05 38 36.0, Dec = -69 05 11, 20' to the north-east of SN1987A), with approximately 7 hours on target. Initial flagging and calibration was performed using tools from the AFRICANUS software ecosystem (Perkins et al. 2025; Kenyon et al. 2025; Bester et al. 2026; Smirnov et al. 2025) with a strategy similar to that discussed in Bester et al. (2026, see § 5.1). The target field was imaged in 53.5 MHz sub-bands and $0'.82 \times 0'.82$ pixels, resulting in a $16 \times 7920 \times 7920$ image covering a 1.8×1.8 field of view and all of L-band. The SARA algorithm in PFB-IMAGING (Bester et al. 2026) was used for deconvolution. Two rounds of phase self-calibration were performed using QUARTICAL (Kenyon et al. 2025), the first after convergence of SARA with the *rmsfactor* parameter set to 3, and the second after convergence with *rmsfactor* set to 1.5. A final round of deconvolution was performed with an *rmsfactor* of 1 using Briggs weighting with a robustness value of -0.5. This resulted in an image with a resolution of about $8''$ at an effective frequency of 1.228 GHz and with an off-source rms of $15 \mu\text{Jy beam}^{-1}$. No primary beam corrections were applied. A portion of the final image is shown in Figure 4 (right panel).

3.10 Data Products

The imaging data products for this survey, available at <https://doi.org/10.48479/jrn4-ga52>, are divided into six overlapping $5^\circ \times 5^\circ$ mosaics as indicated in Table 3. There are two variants of the Stokes I/spectral index cubes, with the first having file names in the format <mosaic>_I_Mosaic.fits.gz (where <mosaic> is the Name root given in Table 3). Both are in the format described in Cotton (2019). The first plane is the broadband Stokes I image at the effective frequency of 1295.05 MHz, the second plane is the fitted spectral index in pixels as described in Section 3.6 and the following planes are the sub-band images with central frequencies given in Table 2. All planes are corrected for primary beam gain. The second Stokes I variant, <mosaic>_I_FitSpec.fits.gz, has the same first two planes as <mosaic>_I_Mosaic.fits.gz but they are followed by least squares estimates for flux density (3), spectral index (4) and the reduced χ^2 of the fit. The polarisation images <mosaic>_<s>_Mosaic.fits.gz (<s> = Q, U or V), are similar to <mosaic>_I_Mosaic.fits.gz except that

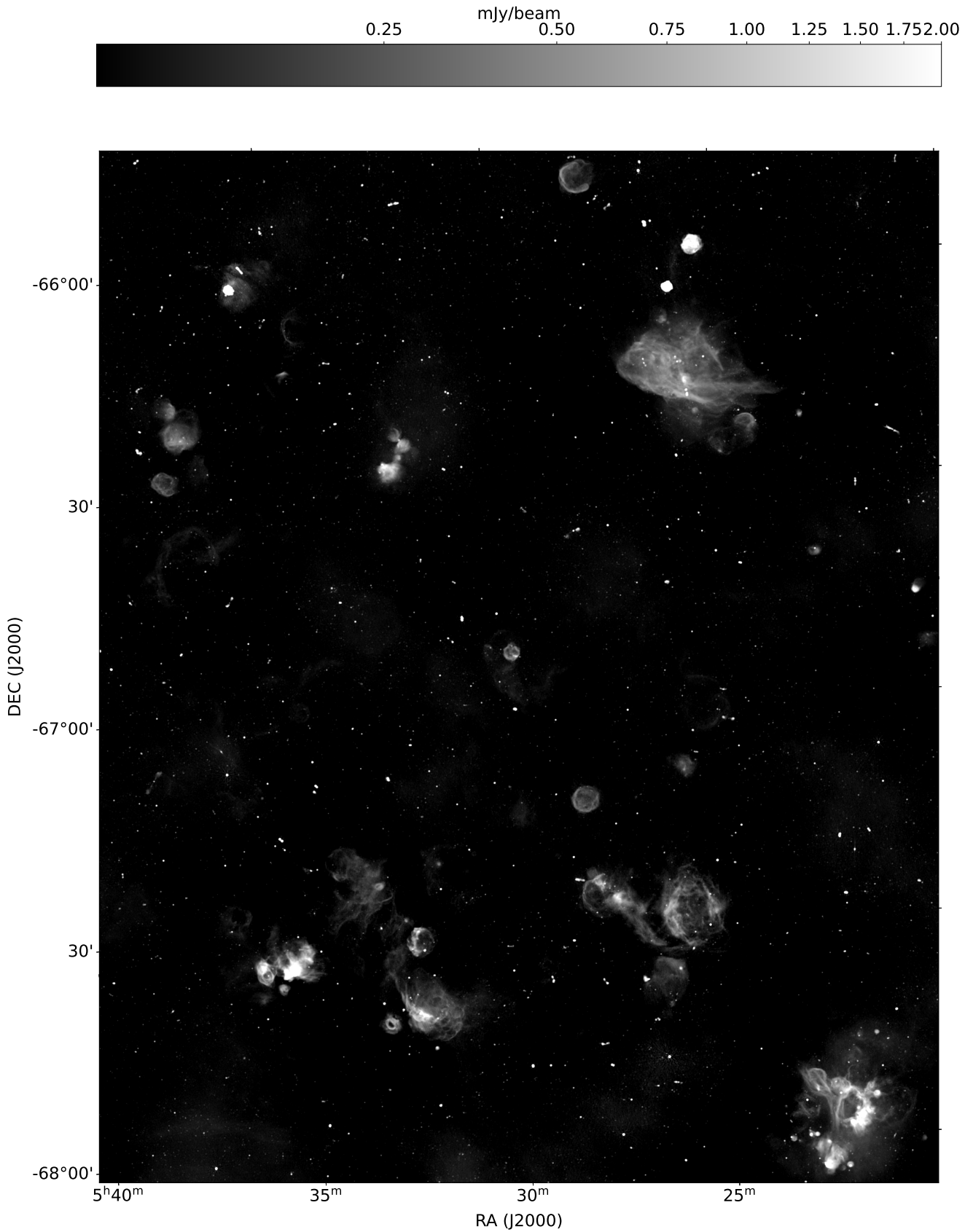


Figure 3. Representative sample of the LMC mosaic. The stretch is inverse hyperbolic sine with range 0.01 to 2.0 mJy beam⁻¹ and is shown in the colourbar at the top. The region displayed is approximately 6.3% of the total mosaic.

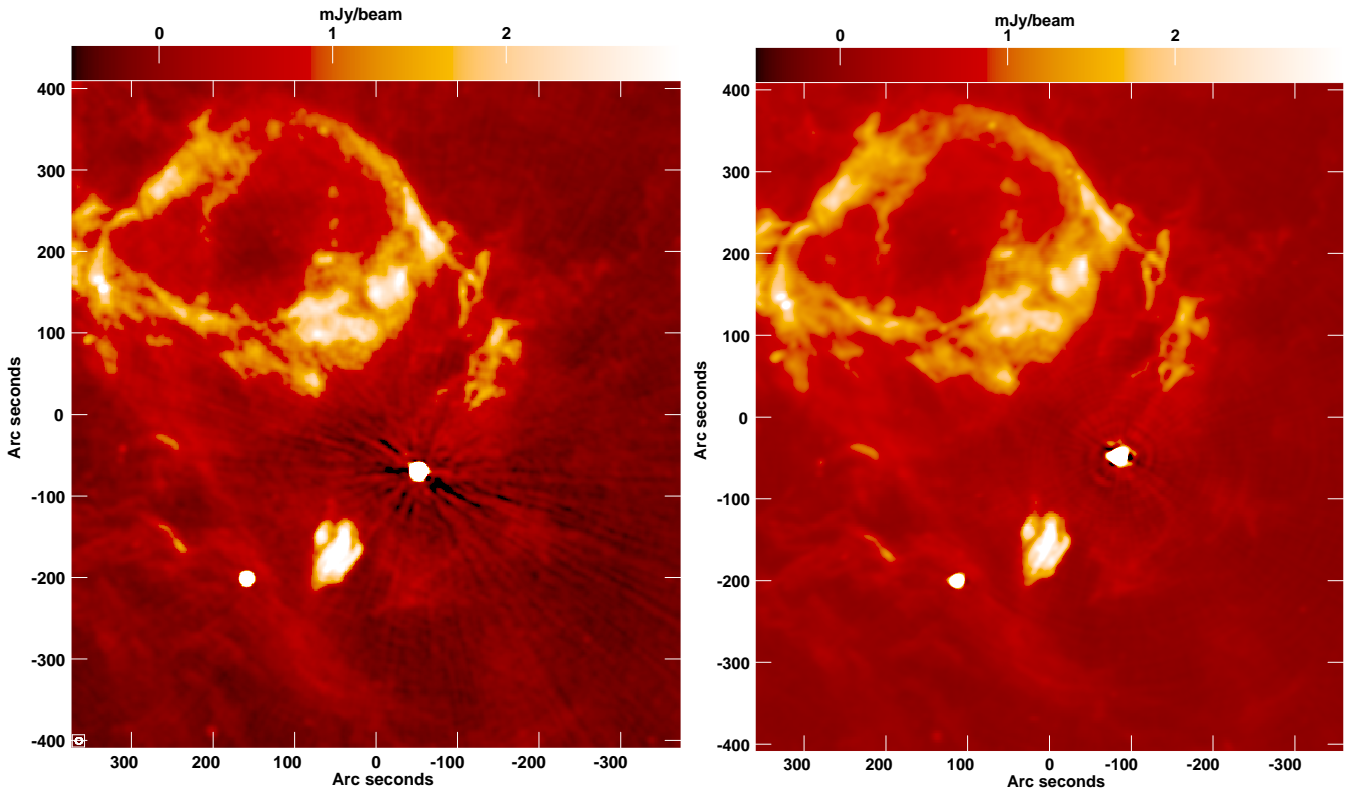


Figure 4. **Left:** The region around SN1987A from the mosaic image based on the LMC survey observations. This field was subjected to peeling which has left visible artefacts surrounding SN1987A, located at RA (J2000)=05 35 28.0, Dec (J2000)=−69 16 12. The linear stretch is given in the scale bar at the top. Coordinates given are relative to the figure centre at RA (J2000)=05 35 39.09, Dec (J2000)=−69 15 08.4. **Right:** The same region on the same stretch from a dedicated observation of 30 Dor, imaged as described in Section 3.9. The longer observation, coupled with more advanced imaging techniques, produces an image with significantly fewer artefacts.

the second plane is blanked. Note that the broadband Q and U images have not been corrected for Faraday rotation and need to be treated with care. The results of the two variants of Faraday analysis described in Section 3.7 are in `<mosaic>_RM_RMSyn_Mosaic.fits.gz` and `<mosaic>_RM_LSQ_Mosaic.fits.gz`. The first three planes of each are 1) RM (rad/m^2), 2) EVPA at $\lambda = 0$ (rad), and 3) peak polarised intensity (Jy). The “RMSyn” cube has a fourth plane, which is the reduced χ^2 of the fit. The “LSQ” cube has least squares errors for RM (plane 4), EVPA (plane 5) and a sixth plane, which is the reduced χ^2 of the fit. Fractional polarisations less than 1–2% of Stokes I should be treated with great caution.

The deep image of 30 Doradus described in Section 3.9 is found in file `30Dor_pfbv0.0.5_sara_prepeel.fits`.

4 HIGHLIGHTED SOURCES

Here we highlight some interesting sources imaged in the MeerKAT LMC survey. These provide a sense of the data quality and potential of the first data release for future investigations. These sources include a range of objects found in the LMC, foreground MW objects, and background extragalactic objects.

4.1 LMC Sources

The LMC has been well-surveyed across the electromagnetic spectrum, from radio, including radio-continuum (Filipovic et al. 1995; Hughes et al. 2007; Pennock et al. 2021) as well as neutral hydrogen

(Kim & ATCA LMC Survey Team 2004; Staveley-Smith et al. 2003) and molecular gas (Fukui et al. 1999; Wong et al. 2011), through IR (Meixner et al. 2006; Meixner 2012), optical (Smith & MCELS Team 1999; Points et al. 2024), UV (Simons et al. 2014; Hagen et al. 2017), X-ray (Pietsch et al. 1996; Haberl 2002), up to high-energy gamma-rays (Ackermann et al. 2016). This allows new survey results to be cross-matched with previous survey data and allows easier multi-frequency analyses of the entire LMC population.

4.1.1 30 Doradus

The 30 Doradus (30 Dor) region in the LMC is the most luminous and energetic star-forming region in the Local Group. In its centre lies the OB association NGC 2070, which contains the dense sub-cluster R 136 at its core, a young (1–2 Myr, Crowther et al. 2016; Bestenlehner et al. 2020) star cluster that contains some of the most massive stars known (Crowther et al. 2010; Brands et al. 2022).

30 Dor consists of three components that have different stellar populations and nebular morphologies (see Figure 5). The A component is simply called 30 Dor, while the other two are commonly referred to as 30 Dor B and 30 Dor C. The high ratio of radio-to-optical emission in 30 Dor B indicates the presence of an SNR, and its flat radio spectrum suggests that the SNR also has a pulsar wind nebula component (Lazendic et al. 2000), similar to the Crab Nebula (Chen et al. 2023). 30 Dor C, discovered by Le Marne (1968) through radio-continuum observation, is one of the brightest non-thermal X-ray and

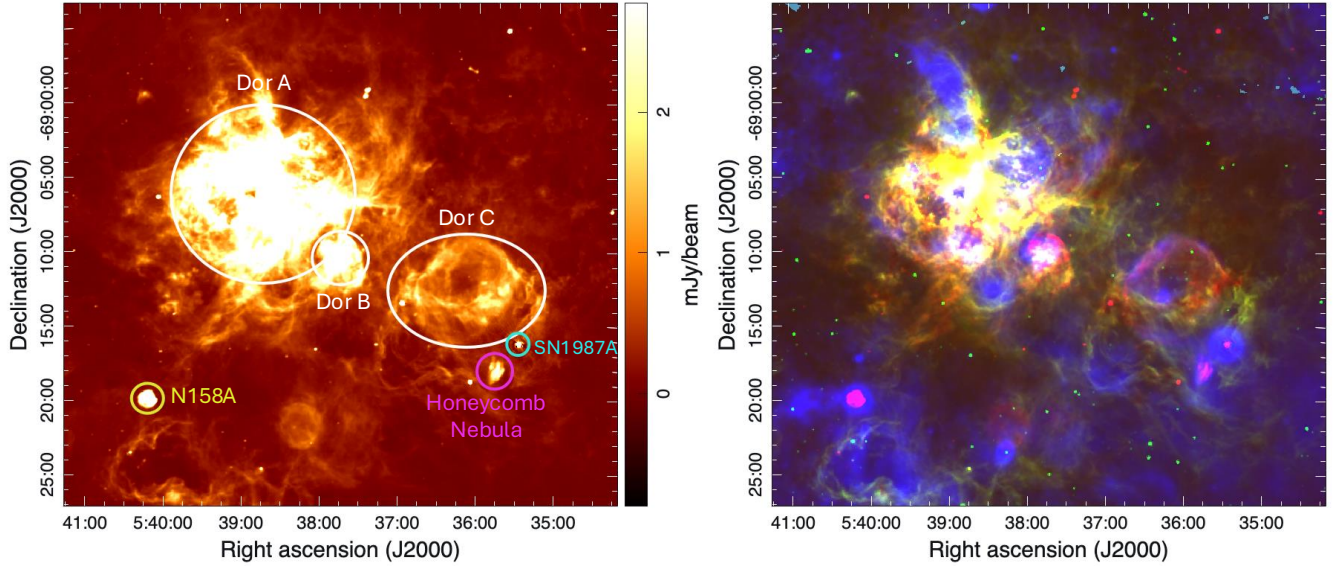


Figure 5. All images in the figure are linearly scaled. **Left:** MeerKAT 1.3 GHz view of the LMC star-forming region 30 Dor, drawn from the image described in Section 3.9. The 30 Dor regions A, B, and C are circled in white, SN1987A is circled in cyan, the Honeycomb Nebula is circled in magenta, and the SNR N158A is circled in yellow. **Right:** RGB composite image of 30 Dor. Red is the MeerKAT 1.3 GHz image, green is an MCELS (Smith & MCELS Team 1999) $H\alpha$ image, and blue is an *XMM-Newton* X-ray 0.3–1 keV image (Maggi et al. 2016).

TeV gamma-ray superbubbles in the Local Group (Kavanagh et al. 2015; Sano et al. 2017; Kavanagh et al. 2019; Yamane et al. 2021).

To the southwest of 30 Dor C are the Honeycomb Nebula, one of the most peculiar SNRs in the LMC (Alsaberi et al. 2024), and the well-known SN1987A (Figure 5).

Several areas of the LMC present radio imaging challenges owing to very bright regions and sources. One of these “difficult” regions surrounds SN1987A. Figure 4 shows a comparison of the imaging obtained through two techniques — the peeling-only mosaic processing described in Section 3.2 and the more advanced technique described in Section 3.9. This demonstrates the sort of improved image quality that can be obtained from the MeerKAT LMC survey underlying data with the use of advanced processing techniques.

4.1.2 Supernova Remnants

The LMC is a prime target for observing SNRs as it is nearby (Pietrzyński et al. 2019) and located away from the Galactic Plane, thus reducing the Galactic absorption that typically complicates the study of Galactic SNRs (Green 2005; Ranasinghe & Leahy 2022). Several studies have been conducted on the SNR population of the LMC (Filipović et al. 2005; Payne et al. 2008; Badenes et al. 2010; Maggi et al. 2016; Bozzetto et al. 2017; Alsaberi et al. 2019; Yew et al. 2021; Filipović et al. 2022; Kavanagh et al. 2022; Bozzetto et al. 2023; Zangrandi et al. 2024; Alsaberi et al. 2025; Ghavam et al. 2025). The most recent (X-ray) survey by Zangrandi et al. (2024) has increased the number of known LMC SNRs to 77 and the number of SNR candidates to 47.

The much improved sensitivity, image fidelity, and resolution of the MeerKAT survey compared to previous LMC studies at ~ 1 GHz provide a new window into the known LMC SNR population. For instance, the MeerKAT image shows the (already) large SNR J0450.4–7050 (also known as J0450–709 and MC 11) to be far larger than previously recognized, owing to the new detection of faint

filamentary features (Smeaton et al. 2025b). A methodical study of the known LMC SNR population using the data products published with this paper promises to be fruitful.

4.1.2.1 Supernova Remnant Candidate The improved sensitivity and image fidelity of the MeerKAT images allow us to discover new SNR candidates. These may have been missed by previous multi-frequency observations due to their low surface brightness or location in complex regions. Following the criteria established in Cotton et al. (2024) and Bozzetto et al. (2023), we searched for circular areas of radio-continuum emission with little to no corresponding optical $H\alpha$ emission. Here we present one such candidate, MCSNR J0455–6925, in Figure 6.

MCSNR J0455–6925 exhibits a circular, bilateral shell in the MeerKAT image, accompanied by a central radio point source. The shell appears to be embedded in a region of more complex diffuse emission. For such a low surface-brightness object, we are unable to measure a reliable in-band spectral index. We detect no corresponding $H\alpha$ emission matching the radio-continuum feature. The large resulting radio-continuum to $H\alpha$ ratio acts as a good indicator for likely non-thermal emission, previously used to identify potential SNR candidates (Cotton et al. 2024; Bozzetto et al. 2023).

We fit a region in CARTA around the candidate and measure a diameter $D = 126''$, and an integrated radio flux density $S = 4.2$ mJy. At the LMC distance of 50 kpc, this gives a diameter of ~ 30 pc and a surface brightness of $\Sigma_{1\text{GHz}} = 1.6 \times 10^{-21} \text{ W m}^{-2} \text{ Hz}^{-1}$, if we assume a typical SNR spectral index of $\alpha = -0.5$. These values fall within typical LMC SNR values, which have a mean diameter of 41 ± 3 pc (Bozzetto et al. 2017), and the diameter and surface brightness combination fall within the Σ – D relation of Bozzetto et al. (2017, their Figure 19).

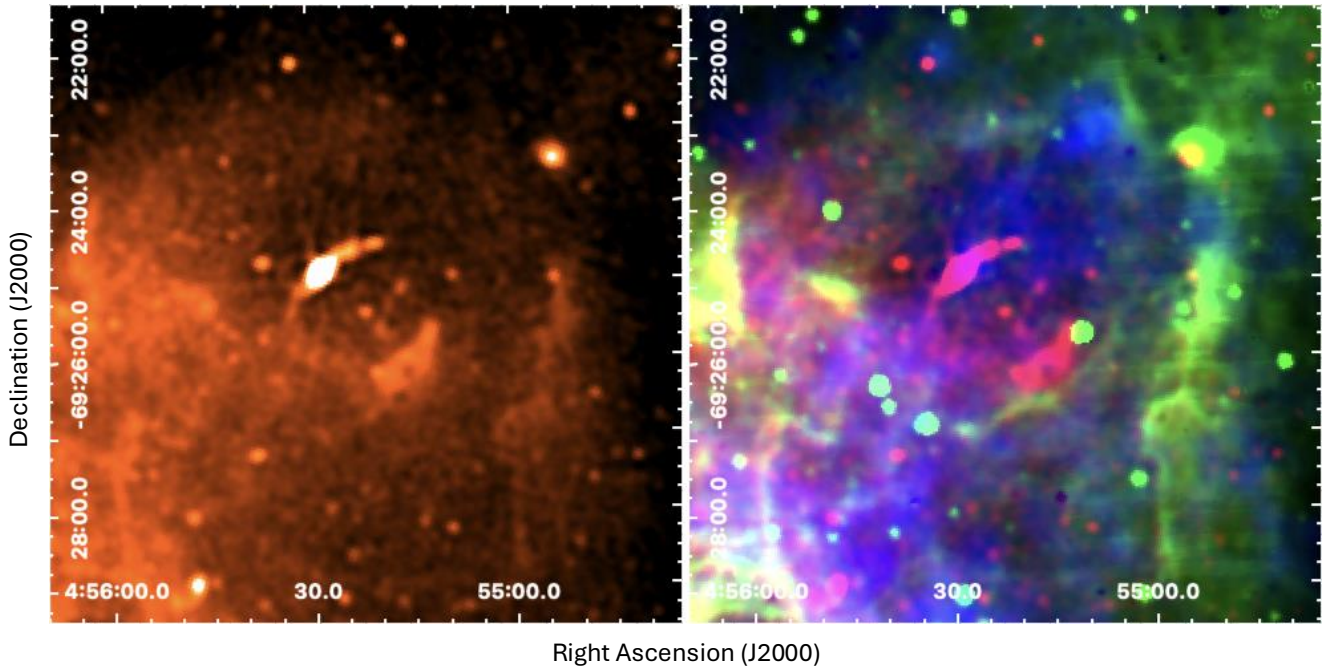


Figure 6. All images in the figure are linearly scaled. **Left:** MeerKAT 1.3 GHz view of the LMC SNR candidate J0455–6925. **Right:** RGB composite image of the LMC SNR candidate J0455–6925. Red is the MeerKAT 1.3 GHz image, green is an MCELS H α image, and blue is an *XMM-Newton* X-ray 0.3–1 keV image.

4.1.3 Planetary Nebulae

There are 431 known PNe within the LMC, identified in optical surveys (Reid & Parker 2010). Approximately 10% of these have confirmed or suspected radio emission (Filipović et al. 2009; Leverenz et al. 2017; Pennock et al. 2021). Radio free-free emission from PNe arises from the electrons in the ionised gas that represents a large fraction of the mass lost during the final stages of the preceding Asymptotic Giant Branch evolution (Zijlstra 1990), which is notoriously difficult to quantify while the star is enshrouded in dust. Higher sensitivity radio images of such objects allow for further investigation into the multi-frequency properties of the LMC PNe population. Several of these known PNe that were not previously detected in radio images now appear in the MeerKAT survey due to its higher sensitivity. We show three such examples in Figure 7: J052218–680239, J051135–681727, and J052147–694315, all identified from their optical emission by Reid & Parker (2006). We measure flux densities of 0.23, 0.06, and 0.20 mJy for each source, respectively. The full set of PNe detected in the MeerKAT images will be presented elsewhere. We expect to detect over 50% of the known LMC population at radio wavelengths and construct the first reliable PNe radio luminosity function.

4.1.4 Wolf-Rayet Stars

Radio detections of WR stars are important due to the fact that the free-free emission can be used to measure mass-loss rates in the winds of these stars, independently from the usual UV (or optical) line profile modelling. Wind clumping is challenging, and radio measurements are less sensitive to it (Abbott et al. 1986; Dougherty et al. 2010). However, the radio spectral index may indicate synchrotron emission, which could arise from colliding winds in binaries.

We used the LMC WR stars catalogue of Neugent et al. (2018) to do an initial search in the MeerKAT images for radio-continuum counterparts to WR stars. Numerous Galactic detections have been made (Abbott et al. 1986; Driessen et al. 2024; Bradley et al. 2025), but the number of extragalactic radio detections of WR stars is still very modest and one of these, PN SMP LMC 83, with a nitrogen-rich WR-type central star, betrays a massive AGB star progenitor that is the radio-loudest PN in its sample (Pennock et al. 2021).

We performed a preliminary search on the MeerKAT LMC mosaic, and report detections of four other WR stars: Brey 3a (6.04 mJy), HD 269687 (0.99 mJy), LHA 120-S 142 (0.29 mJy) and LHA 120-S 61 (2.12 mJy); the quoted integrated flux densities have an estimated 10% uncertainty and their radio-continuum images are shown in Figure 8. The three brightest of these have been detected previously by Pennock et al. (2021), but the faintest source, LHA 120-S 142, is a new detection.

Interestingly, three of these — HD 269687, LHA 120-S 142 and LHA 120-S 61 — are WN11h stars, WR stars that have developed the densest winds; the nature of Brey 3a, irradiating the compact H II region N 82, is uncertain and could involve a WN-type star as well as an interacting binary (van Loon et al. 2010).

A more comprehensive investigation of the MeerKAT images may reveal a more complete population of WR stars in the LMC.

4.1.5 Unclassified Non-Thermal Radio Emission in the Field of the LMC

In Figure 9, we show a prominent non-thermal radio feature located near RA (J2000) = 05 21 20, Dec (J2000) = –68 50 00, about $7' \times 2'$ in size ($\sim 100 \times 30$ pc at the distance of the LMC). No known radio-continuum sources can precisely explain the morphology of this feature, which is exclusively seen at radio-continuum frequencies. We

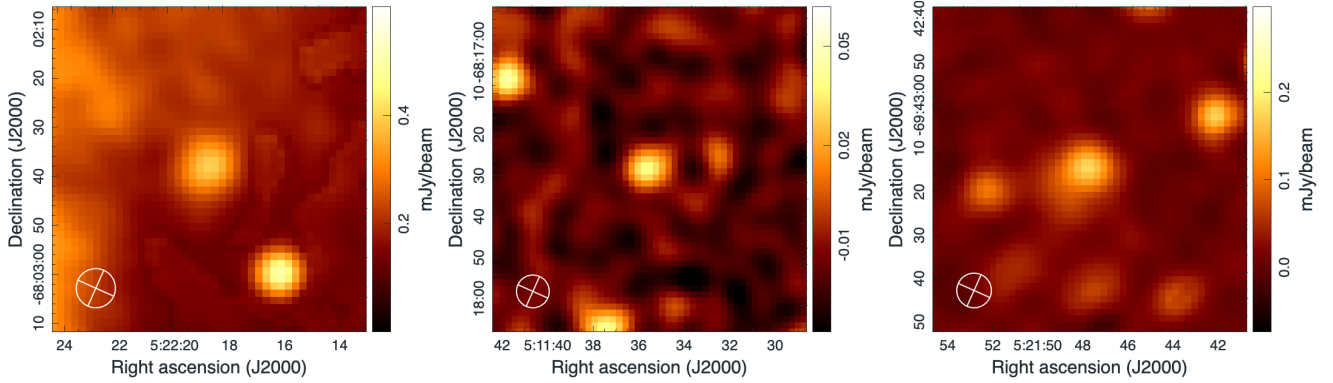


Figure 7. MeerKAT 1.3 GHz view of three LMC PNe previously undetected at radio wavelengths, with the images centred on the optical coordinates of the PNe. From left to right: J052218–680239, J051135–681727, and J052147–694315. The beam size is shown in the bottom left corner. Images are linearly scaled.

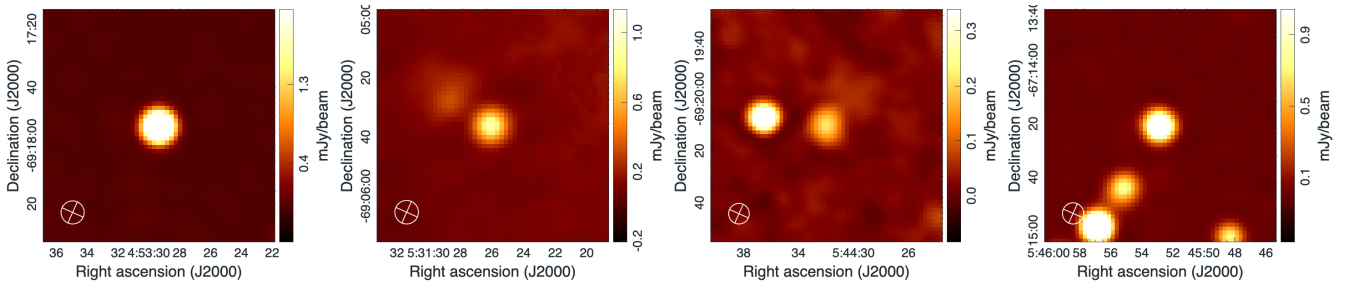


Figure 8. MeerKAT 1.3 GHz view of four LMC WR stars, with the images centred on the optical coordinates of the stars. From left to right: Brey 3a, HD 269687, LHA 120-S 142, and LHA 120-S 61. The beam size is shown in the bottom left corner. Images are linearly scaled.

suggest that it most likely belongs to the LMC due to its morphological appearance. Given its non-thermal nature, found from comparison with optical, IR and X-ray images, this feature could represent an evolved SNR with an extensive NE-to-SW blow-out region; however, we observe no linear polarisation in the MeerKAT data, which argues against this scenario.

There are a broad variety of Galactic non-thermal filaments identified in the SRAO MeerKAT Galactic Plane Survey (SMGPS) (Goedhart et al. 2024), and some appear morphologically similar to this feature. Some of these identified filaments are likely non-thermal in nature, due to the lack of corresponding IR emission; however, a reliable spectral index could not be obtained. The polarisation properties of these SMGPS filaments are also unknown (Goedhart et al. 2024), and thus the lack of observed linear polarisation does not argue against this scenario.

4.2 Foreground Sources

Within the MeerKAT LMC field, we have cross-matched a catalogue of known Galactic stars (obtained from SIMBAD — <https://simbad.cds.unistra.fr/simbad/>) with the LMC MeerKAT point source catalogue (Rajabpour et al. 2026) to identify candidate stars with radio emission at 1.3 GHz.

HD 271037 is detected in both Stokes I and V (see Section 4.2.1),

while two others, HD 27867 (G6V: Høg et al. 2000) and V* U Dor (M8IIIe: Houk & Cowley 1975), are only present in Stokes I. Despite all three having similar 1.3 GHz flux density (0.2–0.3 mJy), only V* U Dor was previously identified as having radio emission (te Lintel Hekkert et al. 1991).

4.2.1 Circularly Polarised Sources

Circular polarisation is present in the radio emission of some stars and most pulsars while extragalactic active galactic nuclei (AGN) and star-forming galaxies are very weakly circularly polarised. The images of the LMC in Stokes V were visually searched to identify sources with circular polarisation. To avoid residual instrumental polarisation, only sources with $|V|/I$ greater than 2% were considered. The 12 sources thus identified are given in Table 4. SIMBAD was used to look for associations with known objects; only one source has no SIMBAD counterpart, and all are likely to be Galactic in origin (in most cases based on parallax, radial velocity and proper motion) except for PSR J0523–7125 located in the LMC.

4.2.2 AB Dor

The low-mass multiple-star system AB Dor was resolved at radio frequencies by Beasley & Cram (1993) and Lim (1993). The MeerKAT

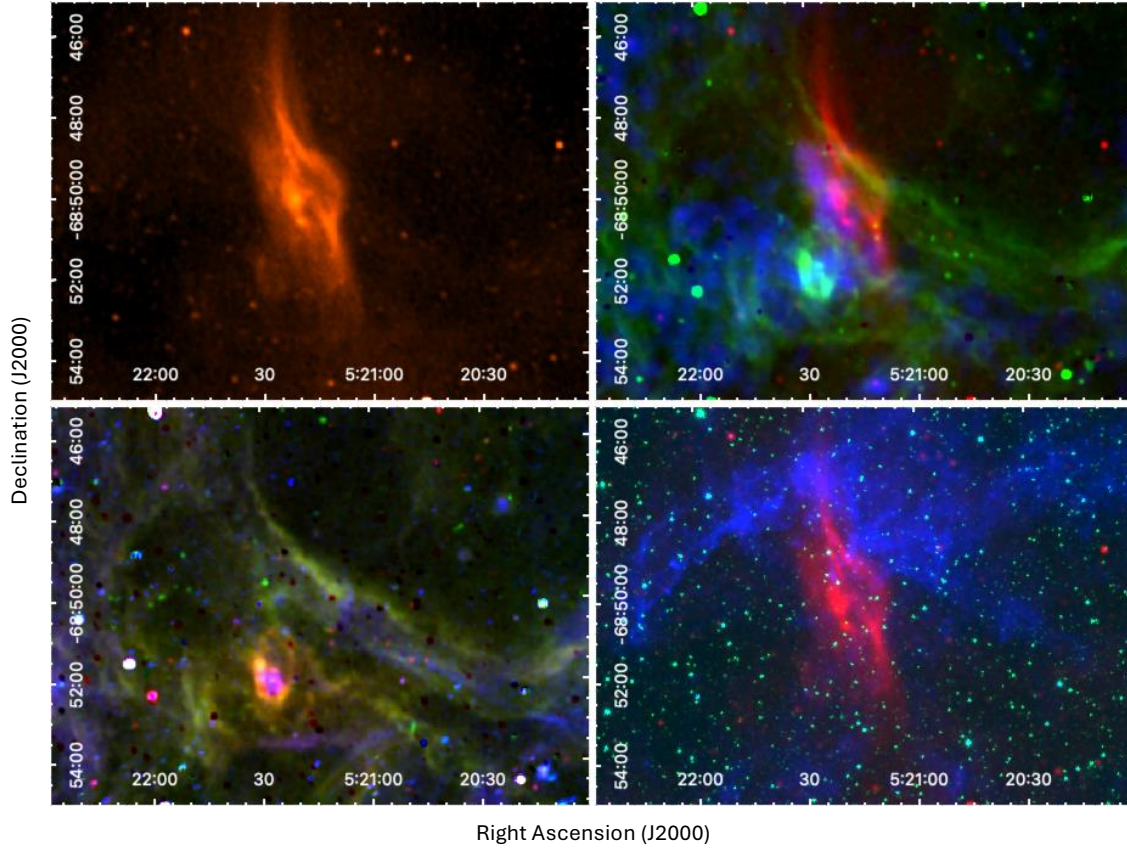


Figure 9. All images in the figure are linearly scaled. **Top left:** MeerKAT 1.3 GHz view of an unclassified non-thermal radio filament in the (field of the) LMC. **Top right:** RGB composite image of filament. Red is the MeerKAT 1.3 GHz image, green is an MCELS $H\alpha$ image, and blue is an *XMM-Newton* X-ray 0.3–1 keV image. **Bottom left:** RGB MCELS optical image of filament area; red is $H\alpha$, green is [S II], and blue is [O III]. **Bottom right:** RGB composite image of radio and infrared observations. Red is the MeerKAT 1.3 GHz image, green is a *Spitzer* 3.6 μm image, and blue is a *Spitzer* 8.0 μm image.

Table 4. Circularly polarised sources in the field of the LMC.

RA (2000)	Dec (2000)	Stokes I $\mu\text{Jy}/\text{beam}$	\pm	Stokes V $\mu\text{Jy}/\text{beam}$	\pm	V/I %	Mosaic	Identification	Comments / references
04 19 13.52	-71 21 12.3	111	7.7	-72	5.0	-65	LMC_SP	RX J0419.2-7120	M4+, multiple ^a , optical flares ^b
04 21 39.29	-72 33 55.1	257	9.0	77	5.0	30	LMC_SP	WOH S 6	M2.5 eruptive variable ^a
04 44 10.69	-70 19 27.8	216	6.9	-115	5.1	-53	LMC_SP	HD 270712B	M1Ve ^c
04 56 23.53	-73 16 38.4	82	7.0	-44	4.7	-54	LMC_S	WOH S 90	M3 ^a
05 00 38.66	-72 52 02.8	91	7.6	-28	4.9	-30	LMC_S	UCAC4 086-008968	^d
05 06 50.53	-72 21 10.5	202	7.2	64	5.1	32	LMC_S	HD 271037	KOIV ^c , eruptive variable star
05 11 17.31	-70 10 00.4	2098	8.4	-56	5.5	-2.6	LMC_S	?	
05 17 03.15	-64 33 15.5	174	8.1	85	6.3	49	LMC_N	WOH G 256	M-type ^a
05 19 57.42	-66 13 55.8	111	11	-59	6.1	-53	LMC_N	HD 269339	G9IV ^c
05 23 48.70	-71 25 52.8	2964	14	493	6.4	17	LMC_S	PSR J0523-7125	LMC pulsar ^e
05 28 45.02	-65 26 52.2	2940	14	-310	8.2	-10	LMC_N	V* AB Dor	See Section 4.2.2
05 40 30.77	-71 25 33.3	198	11	-28	4.5	-14	LMC_S	PSR J0540-7125	Galactic pulsar ^f

^aWesterlund et al. (1981), ^bGünther et al. (2020), ^cTorres et al. (2006), ^dDrissen et al. (2024), ^eWang et al. (2022), ^fD’Amico et al. (1998)

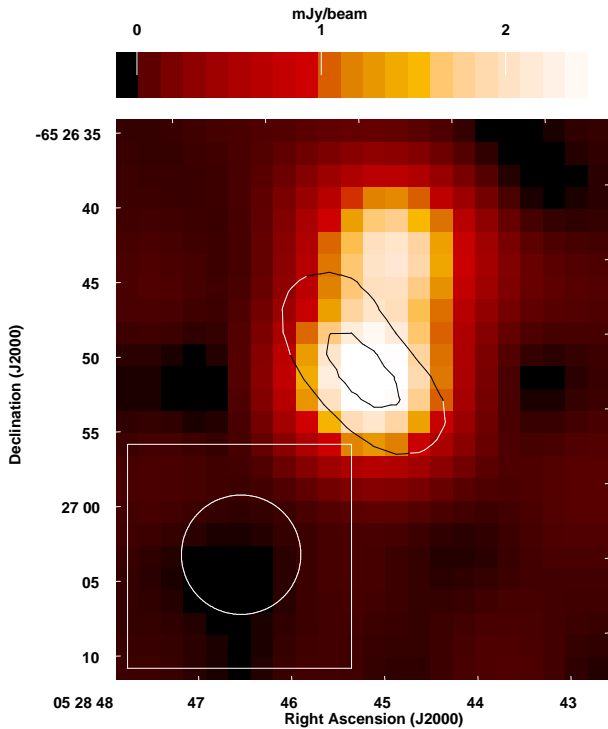


Figure 10. Multiple-star system AB Dor at 1.3 GHz with Stokes I in colour with colourbar at top and Stokes V contours at -100 and $-200 \mu\text{Jy beam}^{-1}$. The resolution is illustrated in the box in the lower left.

image (Figure 10) is now the highest fidelity image of the two main components. The southern component is AB Dor A+C (of which ‘A’, HD 36705, is a K dwarf and ‘C’ a brown dwarf or pair of brown dwarves) and the northern is Rossiter 137B (an M dwarf).

The MeerKAT flux densities appear to be consistent with those reported in the literature. While variability has been reported (Lim 1993), the presence of a quiescent level is too, and we could argue that we are confirming this after a hiatus in observations of three decades. The integrated flux density in the image shown in Figure 10 of the northern component is $2110 \pm 26 \mu\text{Jy beam}^{-1}$ and of the southern (polarised) component is $2940 \pm 26 \mu\text{Jy beam}^{-1}$ (statistical fitting errors).

Reports of circular polarisation are confusing and mixed. Lim et al. (1994) suggest AB Dor A+C is not circularly polarised, so our detection of circular polarisation is interesting, and points to gyro-synchrotron emission, most likely from the fast-rotating, active K-type dwarf. Lim (1993) claims substantial circular polarisation of the M-type dwarf Rossiter 137B, but we do not confirm that here.

This suggests that radio emission from low-mass dwarfs might come from multiple physical components or at least multiple spatial components, and the net radio emission properties are time variable depending on which component dominates at the time of observation.

4.3 Background Sources

4.3.1 Radio Ring Galaxy ESO 084–G014

One of the most intriguing extragalactic sources identified in the MeerKAT LMC survey is the radio ring galaxy ESO 084–G014 (Figure 11). While optical ring galaxies are well studied (Appleton & Struck-Marcell 1996), those with corresponding radio emission are a

relatively new discovery, noted in the MeerKAT SMC survey (Cotton et al. 2024). With a redshift of $z = 0.017$, this galaxy has a physical diameter of 33 kpc (<https://ned.ipac.caltech.edu/>). Optically, it is categorised as an interacting double and is the largest galaxy within its group (Arp & Madore 1987). However, the VISTA survey of the Magellanic Clouds system (Cioni et al. 2011) reveals it to be a face-on spiral galaxy, prominently featuring a central bar and bulge.

The observed radio emission is predominantly concentrated in the spiral arms, with little to no emission located in the central bulge area. The brightest radio emission is observed on the east side and appears to follow the spiral arm structure. As this radio emission is concentrated in the spiral arms, it may be due to areas of enhanced star formation; however, further investigation is necessary to determine the underlying physical processes. MeerKAT’s improved sensitivity and resolution allow a more detailed view of the radio properties of these unusual galaxies and may provide insight into the physical processes of this emission. A detailed analysis of this object and other radio ring galaxies will be presented in Rajabpour et al. (in prep).

4.3.2 EMU EC J041753.5–731556

Another object of interest present in the field is a diffuse circular radio source with a bright central radio source (see Figure 12, left). Originally listed as a radio source in the catalogue of Filipović et al. (2021), the object was later analysed in the 888 MHz Evolutionary Map of the Universe (EMU) survey of the LMC (Pennock et al. 2021) as EMU EC J041753.5–731556. The object was originally catalogued as having a spectral index $\alpha = -1.19 \pm 0.05$ (Filipović et al. 2021). Later, Pennock et al. (2021) found an unusually large spectral index of $\alpha = 5.3$. Pennock et al. (2021) attribute this extreme value to the ~ 20 year epoch difference between the 888 MHz ASKAP data and the 1.384 GHz data from the Australia Telescope Compact Array.

The object has since been observed by the more recent ASKAP EMU survey at 944 MHz (Hopkins et al. 2025, SB59607). This data, combined with the MeerKAT 1.3 GHz data, allows us to re-measure the spectral index and resolve the finer spectral structure. We measure integrated flux densities of 49.7 ± 2.5 mJy (1.3 GHz) and 85.3 ± 4.3 mJy (944 MHz) for the whole object, and 4.6 ± 0.3 mJy (1.3 GHz) and 7.5 ± 0.4 mJy (944 MHz) for the central source. The resulting spectral indices are $\alpha = -1.70 \pm 0.32$ for the entire object, $\alpha = -1.54 \pm 0.38$ for the central source, and $\alpha = -1.71 \pm 0.39$ for the diffuse component (where the diffuse component is taken as the total minus the central source).

These values are in agreement with those measured by Filipović et al. (2021) and indicate a non-thermal origin of the radio emission. The object is not seen in optical, except for the central source, which corresponds with the galaxy 2MASX J04175383–7315568 (Skrutskie et al. 2006). This may be the host of the diffuse radio emission (see Figure 12, right). The galaxy has a measured $z = 0.146$ (Bilicki et al. 2014) corresponding to a Hubble distance of 646 Mpc. The measured angular diameter of $1'.7$ for the diffuse component implies a physical diameter of 270 kpc at the distance of 2MASX J04175383–7315568. These physical properties raise the possibility that EMU EC J041753.5–731556 may be a member of the recently discovered class of radio objects known as Odd Radio Circles (ORCs) (Norris et al. 2021, 2022; Koribalski et al. 2021; Shabala et al. 2024; Smeaton et al. 2025a; Taziaux et al. 2025). ORCs present as circular features of diffuse radio emission that sometimes have a central host galaxy, typically have physical sizes of hundreds

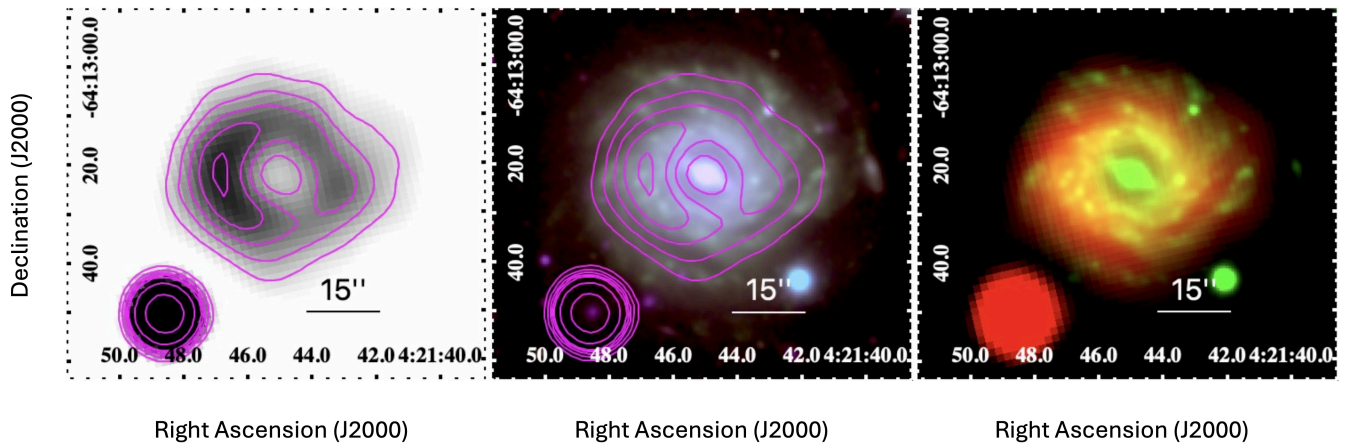


Figure 11. Spiral galaxy ESO 084–G014. The left panel shows the MeerKAT image; in the middle is a DECAM (Flaugher et al. 2015) RGB image (R=z, G=i and B=g band) with MeerKAT contours overlaid; on the right is an RG image of MeerKAT and DECAM (g band). Contours at levels of 100, 150, 200, 250, and 300 $\mu\text{Jy beam}^{-1}$ in the left and centre panels show the MeerKAT 1.3 GHz emission.

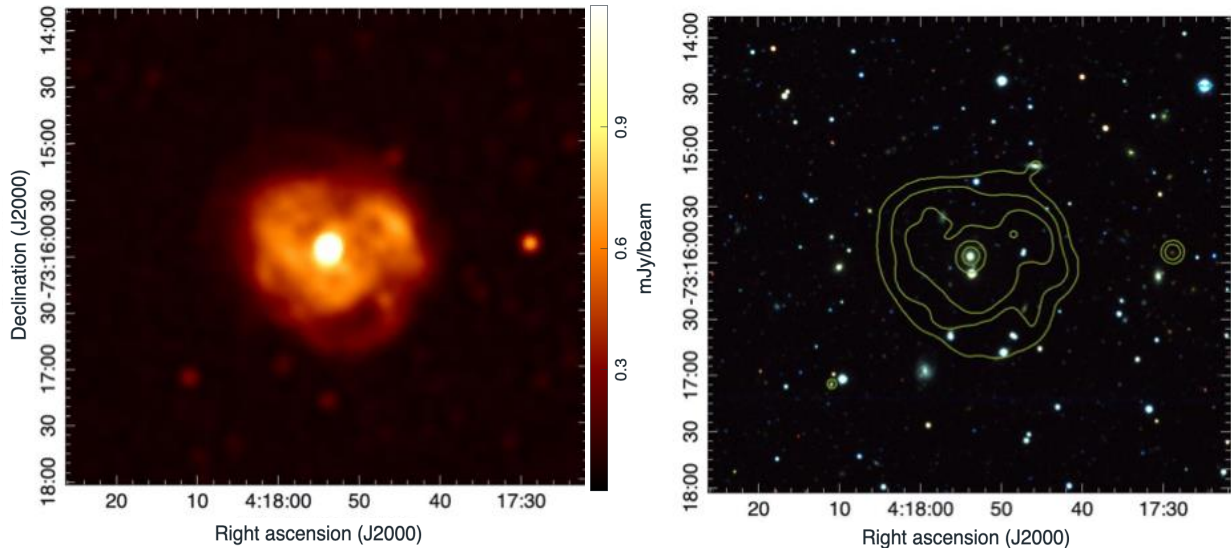


Figure 12. Both images in the figure are linearly scaled. **Left:** MeerKAT 1.3 GHz image of ORC/GLARE candidate EMU EC J041753.5–731556. **Right:** RGB optical image of the EMU EC J041753.5–731556 field from the DESI DR10 Legacy Survey, with the central galaxy 2MASX J04175383–7315568. Red is z-band, green is g-band, and blue is r-band. Contours are from the MeerKAT 1.3 GHz image at levels of 0.1, 0.3, 0.5, 1.0, and 2.0 mJy beam^{-1} .

of kiloparsecs, and are exclusively seen at radio frequencies (Norris et al. 2021).

Recently, Gupta et al. (2025) employed their machine learning (ML) model on this particular EMU field and found a relatively low score for this source, meaning that it did not make it into their top $\sim 1,800$ sources for visual inspection. However, EMU EC J041753.5–731556 might be the first non-ML detected Galaxy with Large-scale Ambient Radio Emission (GLARE; Gupta et al. 2025). As little information is known about the possible host galaxy, and a thorough multi-frequency analysis is outside the scope of this paper, we leave this object as a possible ORC or GLARE candidate to highlight the ability of new radio surveys, such as the one presented here, to help identify and characterise atypical sources.

4.3.3 *Rhodomys*

Figure 13 shows the total intensity 1.3 GHz image, and intriguing jet/lobe morphology, of the bent-tail radio galaxy LEDA 309326, which has been catalogued in optical (Paturel et al. 2003), IR (Huchra et al. 2012; Tully 2015) and radio (Pennock et al. 2021) surveys.

We nickname this galaxy “*Rhodomys*” due to its unusual morphology showing a mouse-like shape with a broader body at the bottom and a long thin trailing tail³.

The MeerKAT image of *Rhodomys*, despite its higher sensitivity,

³ *Rhodomys* is a genus of mouse-like rodent prevalent in Southern Africa (<https://en.wikipedia.org/wiki/Rhodomys>).

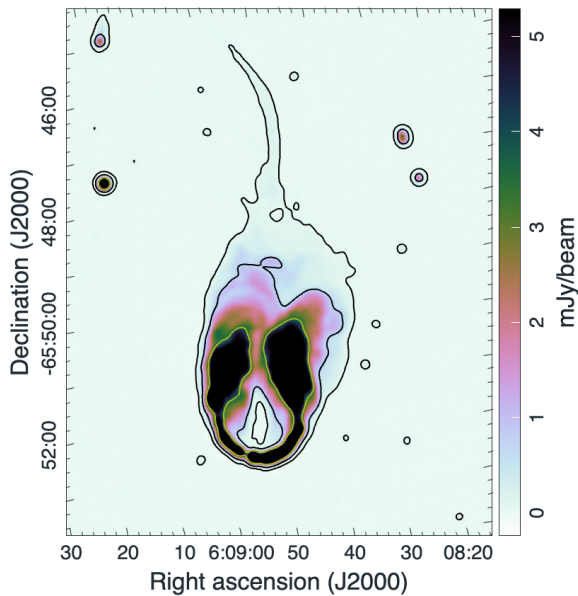


Figure 13. Total intensity MeerKAT 1.3 GHz image of LEDA 309326 (Rhadomys). Image is linearly scaled and contour levels are at $10, 100, 500 \times \sigma$, where $\sigma = 7.5 \mu\text{Jy beam}^{-1}$.

angular resolution, and fidelity, shows broadly comparable features to the ASKAP image at 888 MHz (Pennock et al. 2021). We measure a straight angular distance from the AGN core to the tip of the tail of $8''.0$. This corresponds to a physical size of approximately 350 kpc for the measured $z = 0.037$.

5 CONCLUSION

In this paper, we have presented the MeerKAT 1.3 GHz radio-continuum survey of the LMC, and associated first release of imaging data products. This survey offers significant improvements in resolution, sensitivity to point sources and extended emission, and astrometric accuracy compared to previous radio-continuum surveys of the LMC. Using 258 hours to observe 207 individual pointings, we achieved comprehensive coverage of the LMC with Stokes I rms of $\sim 11 \mu\text{Jy beam}^{-1}$. We have described the calibration, imaging, and mosaicking techniques used to obtain the released data products.

We have also highlighted some results and sources of interest, providing an overview of the broader scientific potential of the full survey. For LMC studies, these data have great utility to study complex regions such as 30 Doradus and the wider ISM, and to study and identify new SNRs, PNe, and Wolf-Rayet stars. In the more distant universe, the great sensitivity to low surface brightness structures and high-fidelity imaging provided by the survey have enabled the identification or fuller characterisation of unusual objects such as a radio ring galaxy and a possible Odd Radio Circle.

ACKNOWLEDGEMENTS

The MeerKAT telescope is operated by the South African Radio Astronomy Observatory, which is a facility of the National Research Foundation, an agency of the Department of Science, Technology and Innovation. The National Radio Astronomy Observatory

and the Green Bank Observatory are facilities of the National Science Foundation, operated under a cooperative agreement by Associated Universities, Inc. This research has made use of the SIMBAD database, operated at CDS, Strasbourg, France. The research of OMS is supported by the South African Research Chairs Initiative of the DSTI/NRF (grant no. 81737).

DATA AVAILABILITY

The raw visibility data are available from the SARAO archive, <https://archive.sarao.ac.za>, under project code SSV-20180505-FC-02. Image products described in Section 3.10 can be obtained from <https://doi.org/10.48479/jrn4-ga52>.

REFERENCES

- Abbott D. C., Beiging J. H., Churchwell E., Torres A. V., 1986, *ApJ*, **303**, 239
 Ackermann M., et al., 2016, *A&A*, **586**, A71
 Alsaberi R. Z. E., et al., 2019, *Ap&SS*, **364**, 204
 Alsaberi R. Z. E., Filipović M. D., Sano H., Kavanagh P., Janas P., Payne J. L., Urošević D., 2024, *Serbian Astronomical Journal*, **208**, 29
 Alsaberi R. Z. E., et al., 2025, *Publ. Astron. Soc. Australia*, **42**, e069
 Appleton P. N., Struck-Marcell C., 1996, *Fundamentals Cosmic Phys.*, **16**, 111
 Arp H. C., Madore B., 1987, A catalogue of southern peculiar galaxies and associations
 Badenes C., Maoz D., Draine B. T., 2010, *MNRAS*, **407**, 1301
 Beasley A. J., Cram L. E., 1993, *MNRAS*, **264**, 570
 Bestenlehner J. M., et al., 2020, *MNRAS*, **499**, 1918
 Bester H. L., et al., 2026, *Astronomy and Computing*, **54**, 100996
 Bilicki M., Jarrett T. H., Peacock J. A., Cluver M. E., Steward L., 2014, *ApJS*, **210**, 9
 Bozzetto L. M., et al., 2017, *ApJS*, **230**, 2
 Bozzetto L. M., et al., 2023, *MNRAS*, **518**, 2574
 Bradley A., et al., 2025, *Publ. Astron. Soc. Australia*, **42**, e101
 Brands S. A., et al., 2022, *A&A*, **663**, A36
 Brunthaler A., et al., 2021, *A&A*, **651**, A85
 Camilo F., Scholz P., Serylak M., et al. 2018, *ApJ*, **856**, 180
 Chen W.-A., Li C.-J., Chu Y.-H., Ueda S., Wang K.-S., Liu S.-Y., Chen B.-A., 2023, *AJ*, **166**, 204
 Cioni M.-R. L., et al., 2011, *Astronomy & Astrophysics*, **527**, A116
 Clarke J. N., 1976, *MNRAS*, **174**, 393
 Cotton W. D., 2008, *PASP*, **120**, 439
 Cotton W. D., 2019, *Obit Memo series*, **63**, 1
 Cotton W. D., et al., 2018, *ApJ*, **856**, 67
 Cotton W. D., et al., 2020, *MNRAS*, **495**, 1271
 Cotton W. D., et al., 2024, *MNRAS*, **529**, 2443
 Crowther P. A., Schnurr O., Hirschi R., Yusof N., Parker R. J., Goodwin S. P., Kassim H. A., 2010, *MNRAS*, **408**, 731
 Crowther P. A., et al., 2016, *MNRAS*, **458**, 624
 D'Amico N., Stappers B. W., Bailes M., Martin C. E., Bell J. F., Lyne A. G., Manchester R. N., 1998, *MNRAS*, **297**, 28
 Dickel J. R., McIntyre V. J., Gruendl R. A., Milne D. K., 2005, *AJ*, **129**, 790
 Dougherty S. M., Clark J. S., Negueruela I., Johnson T., Chapman J. M., 2010, *A&A*, **511**, A58
 Driessen L. N., et al., 2024, *Publ. Astron. Soc. Australia*, **41**, e084
 Filipovic M. D., Haynes R. F., White G. L., Jones P. A., Klein U., Wielebinski R., 1995, *A&AS*, **111**, 311
 Filipovic M. D., White G. L., Haynes R. F., Jones P. A., Meinert D., Wielebinski R., Klein U., 1996, *A&AS*, **120**, 77
 Filipović M. D., Jones P. A., White G. L., Haynes R. F., 1998a, *Publ. Astron. Soc. Australia*, **15**, 128
 Filipovic M. D., et al., 1998b, *A&AS*, **127**, 119
 Filipovic M. D., Haynes R. F., White G. L., Jones P. A., 1998c, *A&AS*, **130**, 421

- Filipović M. D., Jones P. A., White G. L., Haynes R. F., 1998d, *A&AS*, **130**, 441
- Filipović M. D., Payne J. L., Reid W., Danforth C. W., Staveley-Smith L., Jones P. A., White G. L., 2005, *MNRAS*, **364**, 217
- Filipović M. D., et al., 2009, *MNRAS*, **399**, 769
- Filipović M. D., et al., 2021, *MNRAS*, **507**, 2885
- Filipović M. D., et al., 2022, *MNRAS*, **512**, 265
- Flaugher B., et al., 2015, *AJ*, **150**, 150
- Flesch E. W., 2023, *The Open Journal of Astrophysics*, **6**, 49
- For B.-Q., et al., 2018, *MNRAS*, **480**, 2743
- Fukui Y., et al., 1999, in Chu Y. H., Suntzeff N., Hesser J., Bohlender D., eds, IAU Symposium Vol. 190, New Views of the Magellanic Clouds. p. 61
- Ghavam M., et al., 2025, *Serbian Astronomical Journal*, **211**, 27
- Goedhart S., et al., 2024, *MNRAS*, **531**, 649
- Green D. A., 2005, *Mem. Soc. Astron. Italiana*, **76**, 534
- Griffith M. R., Wright A. E., 1993, *AJ*, **105**, 1666
- Günther M. N., et al., 2020, *AJ*, **159**, 60
- Gupta N., et al., 2025, *Publ. Astron. Soc. Australia*, **42**, e097
- Haberl F., 2002, *arXiv e-prints*, pp astro-ph/0203233
- Hagen L. M. Z., Siegel M. H., Hoversten E. A., Gronwall C., Immler S., Hagen A., 2017, *MNRAS*, **466**, 4540
- Heywood I., et al., 2022, *ApJ*, **925**, 165
- Høg E., et al., 2000, *A&A*, **355**, L27
- Hopkins A., et al., 2025, *Publ. Astron. Soc. Australia*, **42**, e071
- Hotan A. W., et al., 2021, *Publ. Astron. Soc. Australia*, **38**, e009
- Houk N., Cowley A. P., 1975, University of Michigan Catalogue of two-dimensional spectral types for the HD stars. Volume I. Declinations -90_ to -53_f0.. Dept. of Astronomy, University of Michigan
- Huchra J. P., et al., 2012, *ApJS*, **199**, 26
- Hughes A., Staveley-Smith L., Kim S., Wolleben M., Filipović M., 2007, *MNRAS*, **382**, 543
- Johnston S., et al., 2008, *Experimental Astronomy*, **22**, 151
- Jonas J., MeerKAT Team 2016, in MeerKAT Science: On the Pathway to the SKA. p. 1, doi:10.22323/1.277.0001
- Joseph T. D., et al., 2019, *MNRAS*, **490**, 1202
- Kavanagh P. J., Sasaki M., Bozzetto L. M., Filipović M. D., Points S. D., Maggi P., Haberl F., 2015, *A&A*, **573**, A73
- Kavanagh P. J., et al., 2019, *A&A*, **621**, A138
- Kavanagh P. J., Sasaki M., Filipović M. D., Points S. D., Bozzetto L. M., Haberl F., Maggi P., Maitra C., 2022, *MNRAS*, **515**, 4099
- Kenyon J. S., Perkins S. J., Bester H. L., Smirnov O. M., Russeeawon C., Hugo B. V., 2025, *Astronomy and Computing*, **52**, 100962
- Khattab O. K., Filipović M. D., Smeaton Z. J., Alsaberi R. Z. E., Crawford E. J., Leahy D., Dai S., Rajabpour N., 2025, *Serbian Astronomical Journal*, **211**, 9
- Kim S., ATCA LMC Survey Team 2004, in American Astronomical Society Meeting Abstracts. p. 93.06
- Kim S., Staveley-Smith L., Dopita M. A., Freeman K. C., Sault R. J., Kesteven M. J., McConnell D., 1998, *ApJ*, **503**, 674
- Kim S., Staveley-Smith L., Dopita M. A., Sault R. J., Freeman K. C., Lee Y., Chu Y.-H., 2003, *ApJS*, **148**, 473
- Knowles K., et al., 2022, *A&A*, **657**, A56
- Koribalski B. S., Norris R. P., Andernach H., Rudnick L., Shabala S., Filipović M., Lenc E., 2021, *MNRAS*, **505**, L11
- Large M. I., Mills B. Y., Little A. G., Crawford D. F., Sutton J. M., 1981, *MNRAS*, **194**, 693
- Lazendic J. S., Dickel J. R., Haynes R. F., Jones P. A., White G. L., 2000, *ApJ*, **540**, 808
- Le Marne A. E., 1968, *MNRAS*, **139**, 461
- Leverenz H., Filipović M. D., Vukotić B., Urošević D., Grieve K., 2017, *MNRAS*, **468**, 1794
- Lim J., 1993, *ApJ*, **405**, L33
- Lim J., White S. M., Nelson G. J., Benz A. O., 1994, *ApJ*, **430**, 332
- Maggi P., et al., 2016, *A&A*, **585**, A162
- Mauch T., Murphy T., Buttery H. J., Curran J., Hunstead R. W., Piestrzynski B., Robertson J. G., Sadler E. M., 2003, *MNRAS*, **342**, 1117
- Mauch T., et al., 2020, *ApJ*, **888**, 61
- Mayer M. G. F., et al., 2025, *A&A*, **700**, A137
- Meixner M., 2012, in American Astronomical Society Meeting Abstracts #219. p. 303.03
- Meixner M., et al., 2006, *AJ*, **132**, 2268
- Mills B. Y., 1985, *Publ. Astron. Soc. Australia*, **6**, 72
- Murphy T., et al., 2010, *MNRAS*, **402**, 2403
- Neugent K. F., Massey P., Morrell N., 2018, *ApJ*, **863**, 181
- Noordam J. E., 2004, in Oschmann Jacobus M. J., ed., Society of Photo-Optical Instrumentation Engineers (SPIE) Conference Series Vol. 5489, Ground-based Telescopes. pp 817–825, doi:10.1117/12.544262
- Norris R. P., et al., 2021, *Publ. Astron. Soc. Australia*, **38**, e003
- Norris R. P., et al., 2022, *MNRAS*, **513**, 1300
- Paturol G., Petit C., Prugniel P., Theureau G., Rousseau J., Brouty M., Dubois P., Cambrésy L., 2003, *A&A*, **412**, 45
- Payne J. L., White G. L., Filipović M. D., 2008, *MNRAS*, **383**, 1175
- Pennock C. M., et al., 2021, *MNRAS*, **506**, 3540
- Perkins S. J., Kenyon J. S., Andati L. A. L., Bester H. L., Smirnov O. M., Hugo B. V., 2025, *Astronomy and Computing*, **52**, 100958
- Pietrzyński G., et al., 2019, *Nature*, **567**, 200
- Pietsch W., Dennerl K., Kahabka P., Pakull M., Schaeidt S., 1996, in Zimmermann H. U., Trümper J., Yorke H., eds, Roentgenstrahlung from the Universe. pp 389–390
- Points S. D., et al., 2024, *ApJ*, **974**, 70
- Rajabpour N., Filipović M. D., Cotton W. D., J. S. Z., Bradley A. C., Crawford E. J., Ghavam M., Khattab O. K., 2026, *MNRAS*, submitted
- Ranasinghe S., Leahy D., 2022, *ApJ*, **940**, 63
- Reid W. A., Parker Q. A., 2006, *MNRAS*, **373**, 521
- Reid W. A., Parker Q. A., 2010, *MNRAS*, **405**, 1349
- Reynolds J. E., 1994, ATNF Memo, AT/39.3/040
- Sano H., et al., 2017, *ApJ*, **843**, 61
- Shabala S. S., et al., 2024, *PASA*, **41**, e024
- Simons R., Thilker D., Bianchi L., Wyder T., 2014, *Advances in Space Research*, **53**, 939
- Skrutskie M. F., et al., 2006, *AJ*, **131**, 1163
- Smeaton Z. J., et al., 2025a, *Publ. Astron. Soc. Australia*, **42**, e119
- Smeaton Z. J., et al., 2025b, *Serbian Astronomical Journal*, **210**, 13
- Smirnov O. M., Tasse C., 2015, *MNRAS*, **449**, 2668
- Smirnov O. M., Makhathini S., Kenyon J. S., Bester H. L., Perkins S. J., Ramaila A. J. T., Hugo B. V., 2025, *Astronomy and Computing*, **52**, 100959
- Smith R. C., MCELS Team 1999, in Chu Y. H., Suntzeff N., Hesser J., Bohlender D., eds, IAU Symposium Vol. 190, New Views of the Magellanic Clouds. p. 28
- Staveley-Smith L., Kim S., Calabretta M. R., Haynes R. F., Kesteven M. J., 2003, *MNRAS*, **339**, 87
- Taziaux S., et al., 2025, *A&A*, **702**, A219
- Tingay S. J., et al., 2013, *Publ. Astron. Soc. Australia*, **30**, e007
- Torres C. A. O., Quast G. R., da Silva L., de La Reza R., Melo C. H. F., Sterzik M., 2006, *A&A*, **460**, 695
- Tully R. B., 2015, *AJ*, **149**, 171
- Wang Y., et al., 2022, *ApJ*, **930**, 38
- Westerlund B. E., Olander N., Hedin B., 1981, *A&AS*, **43**, 267
- White G. L., Filipovic M. D., Jones P. A., Haynes R. F., Wielebinski R., Klein U., 1996, in American Astronomical Society Meeting Abstracts #188. p. 65.05
- Wong T., et al., 2011, *ApJS*, **197**, 16
- Yamane Y., et al., 2021, *ApJ*, **918**, 36
- Yew M., et al., 2021, *MNRAS*, **500**, 2336
- Zangrandi F., et al., 2024, *A&A*, **692**, A237
- Zijlstra A. A., 1990, *A&A*, **234**, 387
- te Lintel Hekkert P., Caswell J. L., Habing H. J., Haynes R. F., Haynes R. F., Norris R. P., 1991, *A&AS*, **90**, 327
- van Loon J. T., et al., 2010, *AJ*, **139**, 68

This paper has been typeset from a $\text{\TeX}/\text{\LaTeX}$ file prepared by the author.